Macromolecules **2001,** *34,* 8944−8952

Real-Time Evolution of the Lamellar Organization of Poly(ethylene terephthalate) during Crystallization from the Melt: High-Temperature Atomic Force Microscopy Study

D. A. Ivanov,*,† Z. Amalou,† and S. N. Magonov‡

Laboratoire de Physique des Polymères, CP 223, Université Libre de Bruxelles,
Boulevard du Triomphe, B-1050 Brussels, Belgium, and Digital Instruments/Veeco Metrology Group,
112 Robin Hill Rd., Santa Barbara, California 93117

Received May 9, 2001; Revised Manuscript Received August 30, 2001

ABSTRACT: High-temperature atomic force microscopy (AFM) was used for in-situ monitoring of melt−crystallization of poly(ethylene terephthalate) (PET) at 233 °C. The observed evolution of the lamellar structure allowed identification of the stack thickening process at the secondary crystallization stage. This finding explains the puzzling decrease of the small-angle X-ray scattering (SAXS) long period observed during isothermal annealing of PET. The quantitative analysis of high-temperature AFM images provides statistically meaningful parameters for the semicrystalline structure and an accurate choice of a structural model for the interpretation of SAXS data.

Introduction

The semicrystalline structure of the typical aromatic polyester, poly(ethylene terephthalate) (PET), has been extensively studied for about 40 years. A significant amount of data has been obtained on the structure and crystallization behavior of PET by various experimental techniques such as small- and wide-angle X-ray scattering (SAXS and WAXS),[1,2] electron diffraction,[3] transmission electron microscopy (TEM),[2,4,5] small-angle light scattering,[6] differential scanning calorimetry,[7] and IR/Raman spectroscopy.[8] However, detailed knowledge of the organization of PET at the nanometer scale and the evolution of its microstructure during crystallization is essentially lacking. This can be partly explained by the fact that pure PET presents a difficult object for TEM studies.[5] As far as the time evolution of the microstructure is concerned, the only conventional technique capable of probing it in real time, i.e., SAXS, is a purely reciprocal space technique, and mathematical modeling is required to extract morphological parameters of the semicrystalline structure from the SAXS data. The results of such modeling can be ambiguous and critically depend on the validity of the structural model adopted. Even for the simplest one-dimensional model, consisting of alternating crystalline and amorphous layers (infinite stack model), the SAXS correlation function analysis leads to an ambiguity in the assignment of the two main distances of the semicrystalline structure: the crystalline lamellae thickness (L_c) and the interlamellar amorphous layer thickness (L_a).

The development of atomic force microscopy (AFM) made it possible to visualize the spherulitic and subspherulitic features of PET.[9] However, AFM imaging of PET in tapping mode at ambient conditions normally does not provide sufficient contrast between the crystalline and amorphous regions, as will be explained in detail in a subsequent paper.[10] To achieve better discrimination between different elements of the semicrystalline morphology of PET, one would need to apply high-temperature tapping mode AFM,[10] allowing imaging at temperatures above the glass transition (T_g). The use of the latter technique is also the only way to perform in-situ studies of PET crystallization, which, for kinetic reasons, is impossible at room temperature. It should be noted that a number of studies have already been dedicated to the in-situ monitoring of crystallization of different polymers at elevated temperatures with AFM.[11,12] However, to the best of our knowledge, the heating stage setups used previously did not allow for correct temperature control during imaging. The main problem in these heating accessories consisted in the fact that, despite the control of the sample and/or sample surface temperature, the tip temperature remained uncontrolled and unknown. However, it is clear that the tip temperature can be extremely important in polymer crystallization studies, where an additional supercooling of the quiescent polymer melt within the tip−sample contact area can result in significant variation of the crystallization conditions and formation of artificial morphological features. In the present paper, we report the first time-resolved studies of isothermal melt crystallization of PET conducted with a precise control of both the sample and tip temperature. Also, the recently developed AFM heating stage accessory used in these studies allows imaging at crystallization temperatures up to 250 °C, which are much higher than those used previously for similar studies. Apart from this pure instrumental improvement, the potential of AFM in the quantitative analysis of the semicrystalline structure is explored. The morphological parameters computed from AFM images are compared with those obtained from SAXS, and it is shown that the direct space AFM information can help in choosing an appropriate model for the interpretation of SAXS data. By combining results of these complementary characterization techniques, more detailed knowledge of the semicrystalline structure of PET is obtained.

---

† Université Libre de Bruxelles.

‡ Digital Instruments/Veeco Metrology Group.

* To whom correspondence should be addressed. Tel +32-2-650-57-59; Fax +32-2-650-56-75; E-mail divanov@ulb.ac.be.

10.1021/ma010809b CCC: $20.00

Experimental Section

Materials. PET was obtained from ICI (grade E47) and was used in experiments without further purification. Size exclusion chromatography measurements of Haubruge et al.[13] performed with a mixture of 1,1,1,3,3,3-hexafluoro-2-propanol (HFIP) and chloroform (2/98 HFIP/CHCl$_3$) as solvent gave the absolute weight- and number-average molecular weights of 42 000 and 19 000, respectively. The samples for AFM studies were prepared by casting PET solutions in HFIP (10 mg/mL) on freshly cleaved mica. The amount of solution deposited on the substrate was chosen to produce films with several microns thickness. The films were dried at room temperature for 30 min, melted for 3 min at 280 °C, and then immediately brought to the temperature of crystallization, T_c.

Methods. The thermal treatments of PET films were performed in situ with a commercial AFM (MultiMode, Nanoscope IIIA, Digital Instruments/ Veeco Metrology Group) equipped with a high-temperature heating stage accessory operated in an atmosphere of He. The design of the heating stage includes a plug-in sample heater and a resistive heater for the probe integrated into the probe holder. To reach the conditions of thermal equilibrium and ensure stable imaging in tapping mode, the temperatures of the sample and the probe were adjusted to be the same. The sample temperature was monitored with a thermocouple positioned in the vicinity of the sample puck, whereas the temperature of the probe was determined from its fundamental resonant frequency. The angular resonant frequency of a rectangular lever without a concentrated load in a vacuum is given by[14]

$$\omega_0 = (1+\beta)\frac{t}{l^2}\sqrt{\frac{E}{\rho_{\text{lev}}}} \tag{1}$$

where t, l, ρ_{lev}, and E are the thickness, length, mass density, and elastic modulus of the lever material and β is a constant approximately equal to 1.498×10^{-2}. From eq 1 it can be seen that the change of ω_0 with temperature can be accounted for by the variation of the elastic modulus of the lever material and the change in the lever dimensions. The latter effect can be expressed in terms of the linear thermal expansion coefficient $\alpha(T)$ as

$$l(T) = l(T_0)\left(1 + \int_{T_0}^{T}\alpha(T)\,\mathrm{d}T\right) \tag{2}$$

Rearranging eqs 1 and 2, one readily obtains

$$\frac{\omega_0(T)}{\omega_0(T_0)} = \frac{1+\int_{T_0}^{T}\alpha(T)\,\mathrm{d}T}{1+2\int_{T_0}^{T}\alpha(T)\,\mathrm{d}T}\left(1-3\int_{T_0}^{T}\alpha(T)\,\mathrm{d}T\right)^{-1/2}\sqrt{\frac{E(T)}{E(T_0)}} \approx \left(1+\frac{1}{2}\int_{T_0}^{T}\alpha(T)\,\mathrm{d}T\right)\sqrt{\frac{E(T)}{E(T_0)}} \tag{3}$$

where $\omega_0(T)$, $E(T)$ and $\omega_0(T_0)$, $E(T_0)$ denote the angular frequency and elastic modulus at temperatures T and T_0, respectively. It can be seen that the decrease of the elastic modulus with temperature and the corresponding increase of the lever dimensions have opposite effects on the resonant frequency. It should be emphasized, however, that the formulas[1−3] are only valid for the case of the cantilever oscillation in a vacuum, without any damping effects. To account for the effectively added mass due to the interaction of the cantilever with the medium, as well as for the cantilever damping due to the medium viscosity, the viscous model in the limit of small dissipative effects can be used.[15] In this case, the resonant frequency of the cantilever immersed in a medium, $\omega_{0,\text{med}}$, will read as follows:

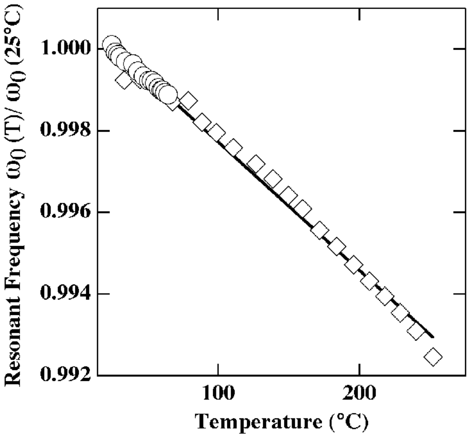

Figure 1. Temperature dependence of the fundamental resonance frequency of a rectangular cantilever used for imaging in tapping mode. Symbols: circles are the data obtained by direct temperature calibration of the resonance frequency by performing frequency sweeps during heating of the head of an AFM; diamonds are the data recomputed from the temperature dependence of the elastic modulus of single crystalline Si in (001) orientation.[16] Solid line is a linear fit to both sets of data.

$$\frac{\omega_{0,\text{med}}}{\omega_0} = \left[1 + \frac{\pi\rho_{\text{med}}b}{4\rho_{\text{lev}}t}\Gamma_{\text{r}}\right]^{-1/2} \tag{4}$$

where ρ_{med} is the mass density of the medium and b is the lever width. The Γ_{r} in eq 4 is a hydrodynamic function[15] depending upon the cantilever geometry and the Reynold's number, Re, which is defined as

$$\text{Re} = \frac{\rho_{\text{med}}\omega b^2}{4\eta} \tag{5}$$

The increase of viscosity, η, diminishes the Reynold's number and results in broadening and low-frequency shift of the relaxation peak. Typical Reynold's numbers corresponding to the real conditions of high-temperature AFM in He atmosphere vary from 3.5 at room temperature and approximately 1.5 at 250 °C. This decrease of Re could bring about a small decrease of the resonant frequency through the function Γ_{r}. However, the increase of temperature leads to the decrease of ρ_{med} and thus to the increase of the resonant frequency. Both effects depend on the choice of the gas atmosphere and are normally small as compared to the temperature variation of the elastic modulus, so that one can write

$$\frac{\omega_{0,\text{med}}(T)}{\omega_{0,\text{med}}(T_0)} \approx \frac{\omega_0(T)}{\omega_0(T_0)} \approx \left(1+\frac{1}{2}\int_{T_0}^{T}\alpha(T)\,\mathrm{d}T\right)\sqrt{\frac{E(T)}{E(T_0)}} \tag{6}$$

Experimentally, the dependence $\omega_0(T)$ was measured within a limited temperature range by placing the head of an AFM in an oven and by performing frequency sweeps at different temperatures. The results of this experiment, shown in Figure 1 in circles, are compared with the resonance frequencies recomputed from the literature data on the temperature-dependent elastic modulus and thermal expansion coefficient of single crystalline Si in (001) orientation[16] (diamonds). It is clear that in the explored temperature range both sets of data superpose and can be approximated by linear dependence. In addition, it was found that the term in eq 6 responsible for the thermal expansion can be neglected for single crystalline Si since it is much smaller than the variation of the elastic modulus. The good agreement between the results indicates that our direct calibration of the probe temperature can be safely extrapolated to a somewhat broader temperature interval. More details on the temperature calibration procedure for this heating stage accessory can be found elsewhere.[17]

SAXS experiments were performed using a rotating anode generator and an evacuated compact Kratky camera equipped with a position-sensitive proportional counter.

Data Processing. The AFM image treatment was performed with home-built routines allowing morphological analysis in both direct and reciprocal space.[18] The images were background corrected by performing the morphological operation of erosion with a small structural element, which effectively removes objects having small size in at least one dimension, such as the crystalline lamellae. The resulting eroded images served as background estimates and were subtracted from the raw images. This flattening procedure is found superior to other types of background corrections since it does not require any a priori assumption about the shape of the background. The analysis of the semicrystalline structure in direct space was performed by automatic analysis of particles encircled by contour lines traced at a certain threshold value of the signal. The threshold was selected using an entropy function to measure the contour line's "fuzziness" (Shannon's entropy function[19]). The thickness was computed for each particle (i.e., crystalline lamellae) as $2S/P$, where S is the surface and P the perimeter of the particle. This expression provides sufficient precision for long lamellar-like objects with a high persistence length (curvature radius) of the contours. To keep certain precision in the thickness determination ($\Delta L_c/L_c \leq \epsilon$) for shorter objects, the latter were sorted with regard to their circularity parameter defined as $P_{\rm circ} \equiv P^2/4\pi S$, and the fraction of objects with $P_{\rm circ} \leq (1+\epsilon)/\pi\epsilon$ was excluded from consideration. The output of the direct-space analysis was a surface-weighted distribution of lamellar thickness.

The analysis of the semicrystalline structure in reciprocal space was performed with the help of a SAXS-type correlation function. The latter was calculated as follows: First, the two-dimensional power spectral density function ($P_2(\underline{s})$) was computed from the images ($u(\underline{r})$) up to the critical, or Nyquist, frequency determined either by the experimental sampling distance or the instrumental resolution:

$$P_2(\underline{s}) = \frac{1}{A}\left|\int u(\underline{r}) \exp(2\pi i \underline{s}\cdot\underline{r}) d^2\underline{r}\right|^2 \qquad (7)$$

where A denotes the image surface area and the reciprocal space vector. The $P_2(\underline{s})$ function was subsequently converted to the one-dimensional form:

$$P_1(s) = \frac{1}{2\pi s}\int P_2(\underline{s}')\delta(|\underline{s}'| - s)\ d^2\underline{s}' \qquad (8)$$

Second, the spectral density was corrected for the presence of the crystal/amorphous transition layers (e.g., sigmoidal-gradient layers[20]) by fitting the large-s tails of $P_1(\underline{s})$ to generalized Porod's law modified for the case of two dimensions:

$$P_1(s) \xrightarrow[s\to\infty]{} \frac{K_P}{s^3} \exp(-4\pi^2 s^2 \sigma^2) \qquad (9)$$

In eq 9, $K_{\rm P}$ and σ denote Porod's constant and the thickness of transition layers, respectively. Third, the $P_1(s)$ function was corrected by a two-dimensional Lorentz factor s, which takes into account the isotropic lamellar orientation. Finally, the SAXS-type one-dimensional correlation function $\gamma(l)_{\rm AFM}$ was calculated as a real part of the Fourier transform of the corrected $P_1(s)$ function:

$$\gamma(l)_{\rm AFM} = {\rm Re}\left[\int P_1(s) \exp(4\pi^2 s^2 \sigma^2 + 2\pi i s l) s\ {\rm d}s\right] \qquad (10)$$

The raw SAXS intensity ($I(s)$) was corrected for absorption, parasitic scattering, detector dead time, and the fluidlike background. The diffraction curves were subsequently desmeared with a variant of Glatter's algorithm[21] and corrected for the electron density transition layers by fitting them to an expression similar to (9) containing the standard three-dimensional scaling law. The SAXS correlation function was then computed as

$$\gamma(l)_{\rm SAXS} = {\rm Re}\left[\int I(s) \exp(4\pi^2 s^2 \sigma^2 + 2\pi i s l) s^2\ {\rm d}s\right] \qquad (11)$$

where s^2 is a three-dimensional Lorentz factor. The SAXS morphological parameters of the lamellar structure of PET, the long period and lamellar thickness, were obtained from $\gamma(l)$ using standard approximate relationships:[22]

$$\varphi_{\rm c,lin}(1 - \varphi_{\rm c,lin})L_{\rm B} = r_0 \qquad (12)$$

$$L_{\rm c} = \varphi_{\rm c,lin} L_{\rm B} \qquad (13)$$

In eqs 12 and 13, $\phi_{\rm c,lin}$ stands for linear crystallinity, $L_{\rm B}$ is determined from the location of the first subsidiary maximum of $\gamma(l)$, and r_0 is the first intercept of the tangent to the linear part of the correlation function in the self-correlation triangle with the abscissa.

Results and Discussion

This section is organized as follows: in the beginning the real-time high-temperature AFM images of the melt crystallization of PET are presented. These observations are further compared with the known models of isothermal crystallization of semirigid chain polymers, and a stack thickening model of the secondary crystallization of PET is put forward. Next, a quantitative comparison between the morphological parameters obtained from SAXS and AFM is performed. In this context, interpretation of SAXS data based on the simple correlation function analysis is specifically addressed. Finally, the problems of quantitative AFM image analysis related to the resolution limitations of the technique and to the 3D to 2D conversion are considered.

Real-Time Isothermal Melt Crystallization of PET. The melt crystallization of PET was conducted at the highest temperature ($T_{\rm c} = 233$ °C) that provided a reasonable rate of crystallization. The AFM experiment was performed by continuously scanning the same surface region at $T_{\rm c}$ for 2.5 h; several selected images of this sequence are given in Figure 2. These micrographs display the time evolution of an area with almost edge-on oriented crystalline lamellae. The crystals appear in the phase images as thin white stripes signifying higher phase signal in the adopted color code, which is in accord with some predictions of the phase response as a function of the set-point amplitude ratio and the elastic modulus of material.[23] An interesting feature in the presented snapshots of crystallization is that the crystalline lamellae manifest a strong tendency to form stacks: Apart from their progressive linear growth, which is typically observed in such experiments, the image sequence in Figure 2 specifically illustrates the stack thickening mechanism of crystallization. The numbers and arrows in the figure help the reader to identify the same lamellar stacks and the same spots on the sample surface. It can be seen that crystallization mainly proceeds by adding crystals parallel to the borders of already existing lamellar stacks, thereby increasing the average number of lamellae per stack (cf. stacks 1 and 2 in Figure 2A–D). Since this mechanism operates after the passage of the main crystallization front (not shown here), it can be referred to as the secondary crystallization.

Models of Isothermal Crystallization. The observed stack thickening mechanism can be important in understanding the results of real-time SAXS experi-

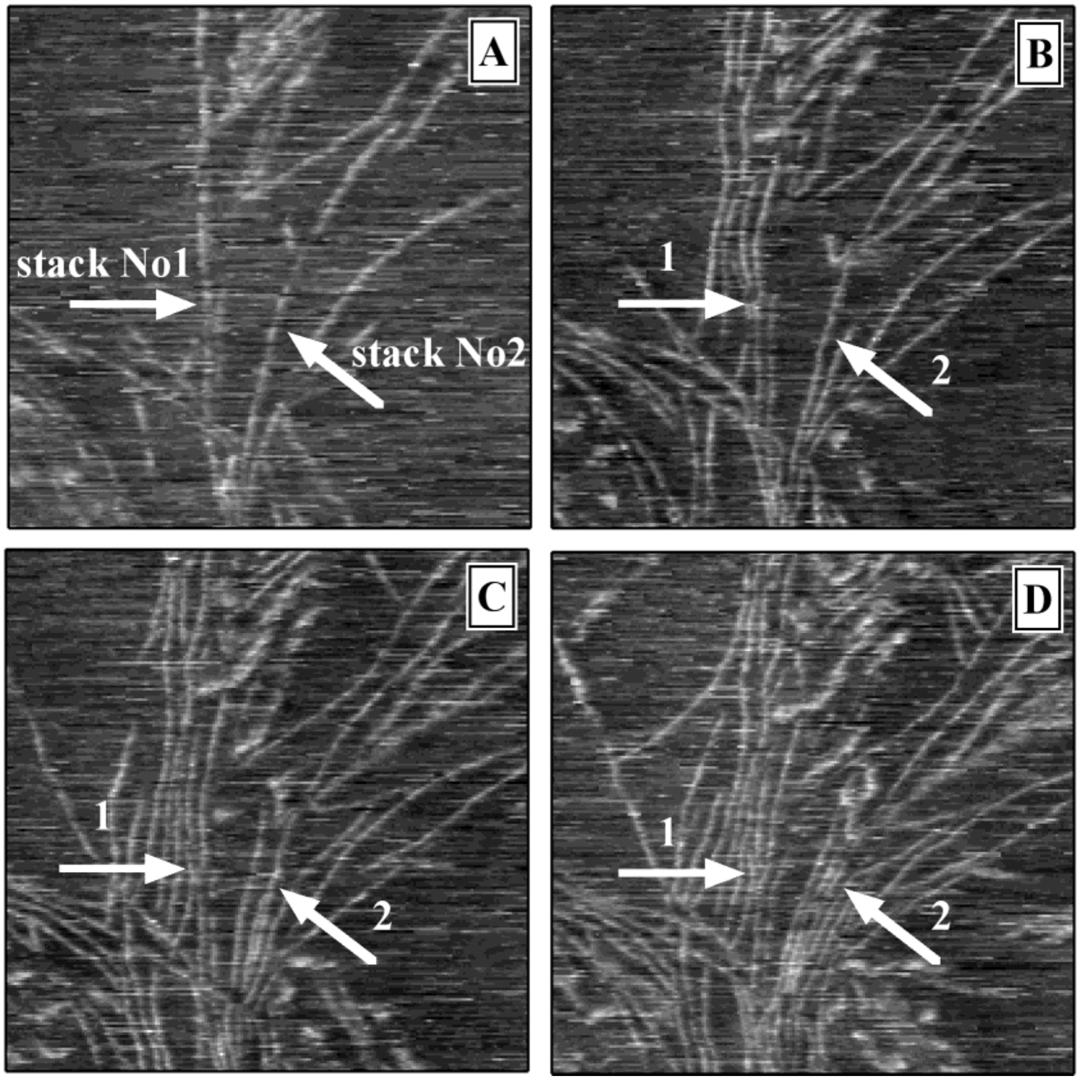

Figure 2. AFM phase images (1 μm^2) recorded in hard tapping during crystallization of PET from the melt at 233 °C; elapsed times are 72 (A), 80 (B), 96 (C), and 112 min (D). Thin white stripes correspond to the crystalline lamellae in almost edge-on orientation. The arrows help the reader to identify the lamellar stacks and the same spots on the sample surface where the crystal growth proceeds via the stack thickening mechanism.

ments. Indeed, one of the puzzling observations made early is the decrease of the SAXS long period during isothermal annealing of PET.[1] The authors[1] suggested that this decrease might be due to the variation of the crystal surface corrugation (Figure 3A), the effect of which on the scattering curves was analyzed by Vonk.[24] Subsequently, two other explanations for this decreasing trend of long period were proposed that are schematically depicted in Figure 3B,C [cf. ref 25 and references therein]. Both explanations are based on the hypothesis of a dual lamellar population, which was designed to rationalize, on one hand, the primary and secondary crystallization stages typically observed during isothermal crystallization of PET and some other semirigid chain polymers and, on the other hand, the well-documented multiple melting behavior. In the first model (Figure 3B) two types of lamellae, the thick and the thin ones, are organized in separate stacks, whereas in the second model (Figure 3C) mixed stacks comprising both types of lamellae are supposed to exist. The advocates of the dual lamellar population suggest that the decrease of the SAXS long period is brought about by the formation of the secondary population of thinner, or more defective, crystals. The latter either insert in between the already existing thick lamellae (Figure 3B) or fill in the not-yet-crystallized, i.e., interstack, regions (Figure 3C).[26] In both cases, the appearance of the secondary, highly imperfect and unstable crystal population is supposed to result from the topological constraints exerted on the amorphous regions by nearby crystals. It is worth noting that, in order to explain the existence of thick crystals, the attribution of SAXS distances obtained from the simple correlation function analysis has to be inverted,[25,27] so that the crystal thickness needs to be associated with the larger of the two distances ($L_c > L_a$). For low and moderate crystallization temperatures, this choice of the crystal thickness causes the L_c distance to become about twice as large as L_a. Evidently, this inverted distance attribution poses a problem for linear SAXS crystallinity which, in this case, significantly exceeds (approximately by a factor of 2) the bulk crystallinity, as determined by standard techniques such as DSC or WAXS. To cope with this problem, the existence of large noncrystallized amorphous regions was also claimed, with the size of these regions estimated to be 200 nm.[25] However, to our knowledge, the existence of either a dual lamellar population or large amorphous gaps persisting in the semicrystalline structure after the completion of crystallization has not been verified experimentally yet.

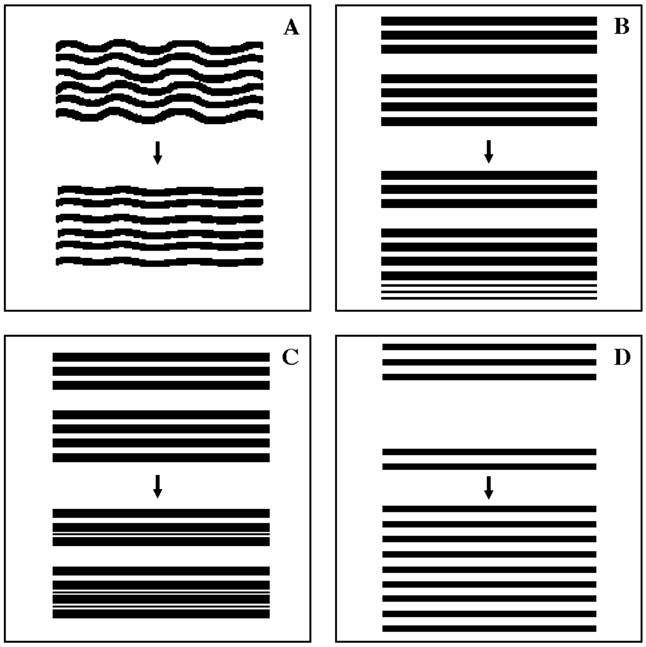

Figure 3. Schematic diagrams of the lamellar microstructure evolution during isothermal crystallization: (A) Model with varying lamellar corrugation;[1] see text for details. (B, C) Dual lamellar population model [ref 25 and references therein] containing separate stacks of thick and thin lamellae (B) and mixed stacks comprising both types of lamellae (C). In this model the linear crystallinity in the stack is significantly higher than the bulk crystallinity. To account for this difference, large amorphous gaps are supposed to exist in the structure. (D) Stack thickening model proposed in the present work. The crystal growth generates a fully space-filling semicrystalline structure, where the value of linear crystallinity matches the bulk crystallinity.

Stack Thickening Model of PET Crystallization. On the basis of our high-temperature AFM results, a fourth, stack thickening, model of secondary crystallization (Figure 3D) can be put forward to explain the described evolution of the SAXS long period. As is generally known, the lamellar microstructure of semicrystalline polymers can contain many stacking defects, which give rise to poor diffraction patterns displaying only one order of diffraction. A simple structure factor calculation for the finite stack model shows that in the presence of the second-order defects in the structure, i.e., paracrystallinity, the SAXS long period can be affected by the number of lamellae per stack.[28] In this case, the effective value of long period obtained from the classical correlation function analysis clearly shows a decreasing trend with the increase of the number of lamellae per stack,[28] which is in qualitative agreement with results of real-time SAXS experiments. To decide whether the proposed stack-thickening model should incorporate one, two, or more crystal populations, the time evolution of the crystal thickness distribution should, in principle, be found. Such information was gained from a detailed direct-space analysis of AFM images, the results of which are summarized in Figure 4. It is seen that the apparent crystal thickness distributions[29] do not make it possible to detect the formation of a second crystal population. Moreover, no systematic time evolution of the shape of these functions can be seen: All distributions are monomodal, the standard deviations being less than approximately 1 nm (Figure 4). The average value of the lamellar thickness, which is about 10 nm, stays almost constant with crystallization time in the time scale of the experiment (Figure 4). It should be noted, however, that the fraction of the secondary crystals is a priori unknown. Thus, to exclude the possibility that the secondary lamellar population was overlooked in this analysis due to insufficiency of the counting statistics, further analyses were performed. To detect this possibly missing crystal population, it was decided, first, to increase the number of analyzed PET crystals and, second, to inspect the semicrystalline morphologies formed after long-time crystallization at the studied temperature.

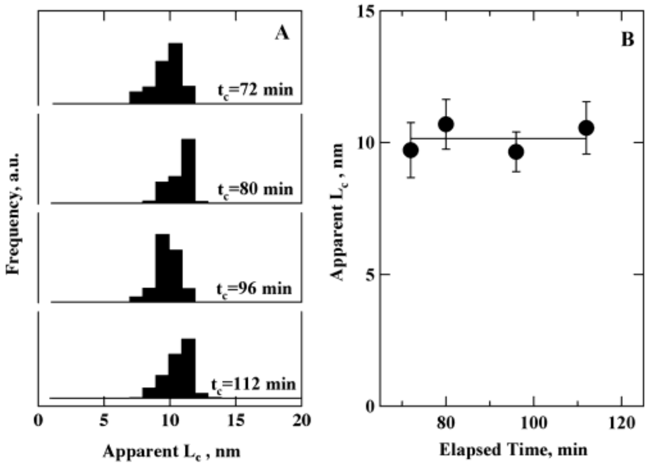

Figure 4. Evolution of the apparent crystal thickness distribution (A) and the average crystal thickness (B) computed from the images given in Figure 2. The error bars in (B) indicate the standard deviations of the distributions.

A representative space-filling semicrystalline morphology of PET corresponding to the completion of crystallization at 233 °C is shown in Figure 5A. A part of this image (boxed area in Figure 5A) with a clearly resolved lamellar structure (Figure 5B) was used for the computations. In Figure 5c the distribution of the apparent crystal thickness for this image is compared to the one corresponding to the last image of the real-time study (Figure 2D). It is clear that the shape and positions of the maxima of both functions are close. Similar results were obtained on other images of a completely crystallized PET sample. Concluding, the hypothesis of the secondary crystallization of PET producing more defective (thinner) crystals has not found support in our experiments. However, we cannot completely rule out that the melt crystallization of PET conducted at such high temperature is not paralleled by segregation of chains containing, for example, some structural defects; these segregated chains could crystallize at a slower pace to form thinner crystals. However, if this hypothetical fraction of thinner crystals were mainly responsible for the low-temperature melting endotherm, it would have been detected in our analysis since the amplitude of this endotherm steadily increasing with crystallization temperature becomes significant for crystallization at 233 °C. It is worth mentioning that, for the case of the cold crystallization of PET, the decrease of the SAXS long period[1] and appearance of the low-temperature endothermic peak cannot be produced by segregation due to the sluggish chain mobility.

Comparison of AFM and SAXS: Attribution of the Two SAXS Distances. To go a step further and address the problem of the assignment of the two SAXS distances resulting from the correlation function analy-

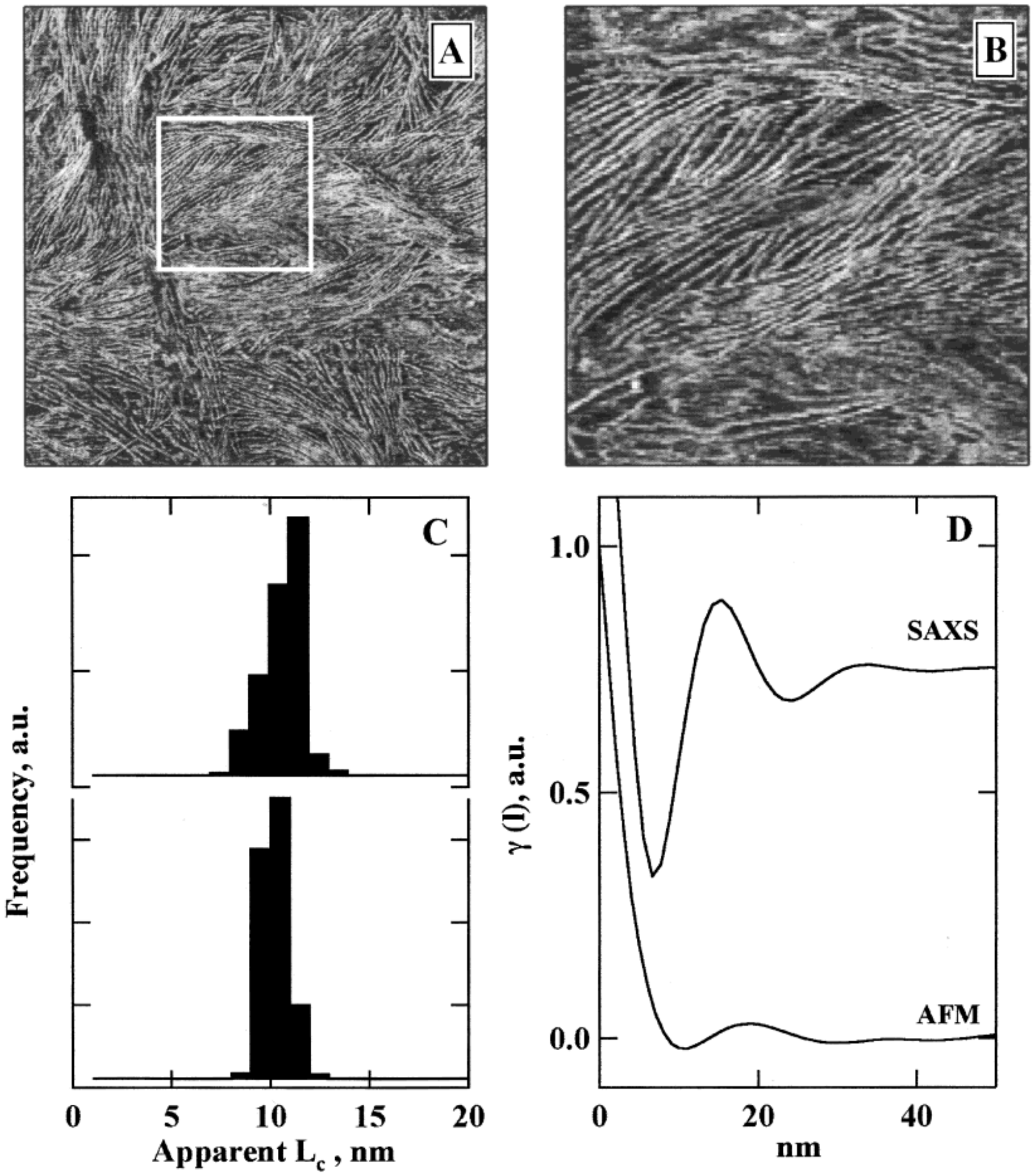

Figure 5. (A, B) Semicrystalline morphology of PET after completion of crystallization at 233 °C. AFM phase images measured at the temperature of crystallization: 9.0 μm^2 (A) and 1.0 μm^2 (B). Image (B) gives a closer view of the boxed region in (A). (C, D) Quantitative analysis of the semicrystalline morphology of PET. (C) Distributions of apparent lamellar thickness corresponding to the images 2d (upper histogram) and (B) (lower histogram). (D) One-dimensional correlation functions computed from AFM and SAXS data; the curves are vertically offset for clarity.

sis, a reciprocal space treatment of high-temperature AFM images has been done. The one-dimensional correlation function obtained from the AFM image of a completely crystallized sample (Figure 5B) is shown in Figure 5D. The SAXS correlation function corresponding to a sample crystallized in the same conditions is given for the sake of comparison. It can be seen that the values of long period ($L_B \equiv L_c + L_a$) determined from the location of the first subsidiary maximum of the correlation function show a reasonable agreement between SAXS and AFM: The AFM and SAXS values are found to be 19.2 and 15.5 nm, respectively. This fact ensures that the morphological parameters of the semicrystalline structure determined by these two very different techniques are comparable.[30] It is instructive to calculate the AFM linear crystallinity, which can be used to choose an appropriate structural model for the interpretation of SAXS. Using the results of the direct space analysis described above, one obtains:$\varphi_{c,lin} \cong 10/19.2 = 0.52$; the corresponding SAXS values are equal to either 0.39 or 0.61. It is clear that the AFM linear crystallinity is intermediate between the two possible SAXS values, which would formally render the choice impossible. However, as will be shown later, the AFM linear crystallinity can be somewhat overestimated, which will leave out the choice of the inverted SAXS distance attribution (i.e., $L_c > L_a$). It is also clear that, at this very high crystallization temperature, the bulk and linear crystallinities should be close to the highest values attainable for PET.[31] By considering the AFM value as the upper bound for the linear crystallinity, one can conclude that for all other crystallization temperatures the linear crystallinity of PET should always be less than 0.5. This is, indeed, what was found in high-temperature AFM studies performed on PET samples crystallized at lower temperature (data not reported here). Thus, it would be possible to reconcile the bulk of high-temperature AFM results only with the choice of crystal thickness as the smallest distance, i.e., $L_c < L_a$.

The discrepancy between the SAXS and AFM values of the morphological parameters needs to be commented on further. While the possibilities and limitations of SAXS in studies of polymers are well-known,[32] similar analysis has not yet been done for the quantitative interpretation of AFM images of the semicrystalline structure. In this respect, two important issues have to be discussed: the first concerns the limited spatial resolution of AFM and its influence on morphology, and the second concerns the problem of the 3D to 2D conversion in the quantitative analysis of AFM images. Both issues, also raised by the referees, will be addressed in the following sections of the paper.

Imaging Resolution for AFM and Its Impact on the Morphological Parameters of the Semicrystalline Structure. The questions related to the spatial resolution for AFM were studied in detail by a number of authors.[33,34] Briefly, the resolution limitations stem from (i) the discretization and limited size of images, represented by two-dimensional arrays of pixels, (ii) the finite probe size resulting in the dilation of topographical features, and (iii) the contact mechanics of imaging leading to the deformation of the sample (and probe) and formation of a finite contact area.

The first problem is trivial and would not need to be discussed here in detail. It should only be noted that, for image treatment in reciprocal space, correct windowing has to be applied, and the critical frequency should be respected to avoid aliasing.

The second problem, however, cannot be circumvented as simply as the first one, i.e., by changing the image size or sampling frequency. The steep topographical features would be distorted irrespective of the pixel size employed in the experiment. In the approximation of a hard surface and a hard spherical tip (i.e., absence of indentation), a feature with height h will appear dilated by about $\sqrt{2Rh}$, where R is the tip curvature radius and $h \ll R$. Thus, it is clear that the objects delimited by steep slopes such as the crystalline lamellae can appear in the images larger than they really are. Since the structure periodicity (e.g., long period) is not affected by this tip-induced dilation, the AFM linear crystallinity can be artificially increased if the crystals protrude from the sample surface. For the high-temperature AFM images reported in this work, the topographical undulations associated with the PET lamellar structure are insignificant. Taking a typical tip apex diameter for etched Si probes in the range of $10 < 2R < 17$ nm, which can be simply checked by measuring some known standards, the resulting dilation is estimated to lie in the 2−2.5 nm range. Therefore, the described dilation effect could result in the overestimation of the linear crystallinity by about 0.1, which would explain the difference between the SAXS and AFM values.

The third source of resolution limitation was analyzed in detail in ref 33. On the basis of Hertzian mechanics, the smallest tip−sample contact area for AFM operation in contact mode was predicted to be about 2−3 nm. The formation of a finite contact area is expected to decrease the sharpness and resolution of structural features. In the image treatment procedure employed in the present work, this effect is largely eliminated by correcting the spectral density function for the presence of transition layers. Thus, as long as the radius of the contact area remains reasonably small (i.e., much smaller than the size of the examined surface features), it is not expected to modify the morphological parameters of the semicrystalline structure.

Generally, the utility of working at high resolution in tapping mode AFM is proved by the fact that structures of a few nanometers in size are commonly seen in AFM images. For example, the clusters of 4−5 resolved particles corresponding to single starburst macromolecules were reported in ref 35. Other examples including images of closely packed nanometer-scale objects can be found in a recent review.[34] Finally, the agreement between the dimensions of crystalline features lying flat-on (height measurement) and standing edge-on (lateral measurement) testifies to the reliability of the quantitative estimation of the parameters of a semicrystalline structure.

The 3D to 2D Conversion Problem in the Quantitative Analysis of AFM Images of the Semicrystalline Morphology. The problem of the structure factor modification in AFM images due to the 3D to 2D conversion was addressed in a recent publication,[36] where the authors compared the kinetics of spinodal decomposition of a polymer blend obtained with a 2D (AFM) vs 3D (light scattering) technique. A similar problem arises in comparative studies conducted with AFM and SAXS. Therefore, analyzing the difference between the AFM and SAXS values of long period (SAXS L_B is about 24% smaller than the corresponding AFM value), one could question the possible inclination of PET crystals with respect to the image plane. Indeed, while SAXS naturally probes the distances along the normal to the basal planes of the stacked lamellae, the orientation of crystals visualized by AFM can be random. Therefore, for all nonzero inclination angles the apparent distances between the adjacent crystals calculated from AFM images are overestimated:

$$L_{\mathrm{B,apparent}} = \frac{L_{\mathrm{B}}}{\cos\varphi} \qquad (14)$$

where ϕ is the angle between the normal to the crystal plane and the plane of the image. For totally isotropic crystal orientation the distribution of long periods found from AFM images will be asymmetrically broadened, with the average distance being shifted toward higher values. The AFM technique obviously does not offer the possibility of directly measuring the tilt of the lamellar crystals in the images; however, discrimination between the stacks oriented close to the edge-on orientation and those inclined at significant angles can easily be made. The image of the semicrystalline structure of PET shown in Figure 6 presents an example of mixed crystal orientation, where both flat-on and edge-on grown crystals are visible. The arrows in the figure point at lamellar stacks with different inclination; the directions of arrows are perpendicular to that of the lamellar stacking, and their lengths are roughly proportional to the apparent crystal periodicity. It can be seen that for lamellar stacks inclined at considerable angles (cf. oblique stack no. 3 with almost flat-on (no. 2) and edge-on (no. 1) oriented stacks in Figure 6) the crystal appearance is radically changing. In this case the details of the crystal habit, i.e., the crystalline facets or the growth front curvature, become visible, indicating the crystal inclination. Therefore, the inspection of lamellar shapes makes it possible to rapidly sort out the stacks inclined at large angles. The discrimination of remaining stacks can be made based on determination of the

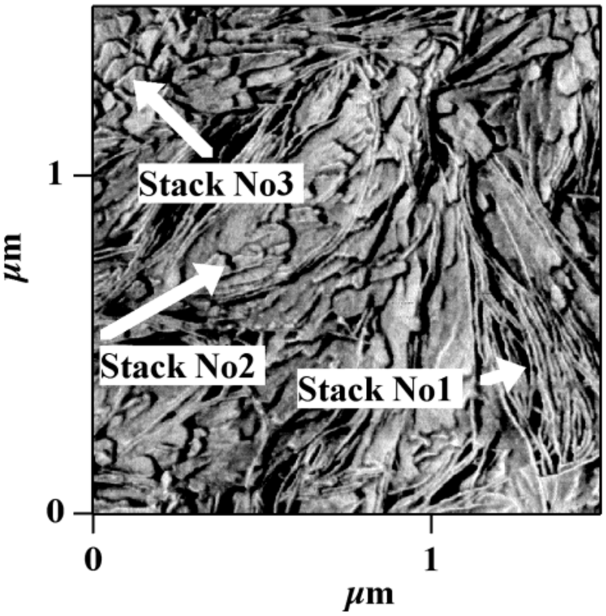

Figure 6. AFM image showing PET semicrystalline structure with mixed orientation of lamellar stacks (room-temperature measurement). The arrows in the figure point at the stacks inclined at different angles; the directions of arrows are perpendicular to that of the lamellar stacking, and their lengths approximately proportional to the apparent crystal periodicity.

long period for each stack. For this purpose one or more AFM images can be divided into fragments and treated separately in order to find the minimum apparent intrastack periodicity, which would be pertinent to a stack with an edge-on orientation. The morphological parameters found from this analysis are supposed to be comparable to the values found from SAXS, assuming the resolution limitation of AFM imaging does not prevail (see the above discussion).

Summarizing, further studies are required to investigate the discrepancies between the morphological parameters of the semicrystalline structure determined by AFM and SAXS. At the present stage, these discrepancies are tentatively attributed to the resolution limitation for AFM, to uncertainties related to the calibration procedures utilized by each of these techniques, and to possible differences in the sample preparation.[37]

Conclusion

High-temperature atomic force microscopy was used to monitor the melt crystallization of poly(ethylene terephthalate) at 233 °C. The observed evolution of the lamellar structure allowed identification of the stack thickening process at the secondary crystallization stage. This finding explains the puzzling decrease of the SAXS long period observed during isothermal annealing of PET. Generally, it is shown that the quantitative analysis of high-temperature AFM images provides meaningful parameters for the semicrystalline structure and an accurate choice of a structural model for the interpretation of SAXS data. Some discrepancies between the morphological values found from SAXS and AFM are tentatively attributed to the resolution limitation for AFM, to uncertainties related to the calibration procedures utilized by each of these techniques, and to possible differences in the sample preparation.

Acknowledgment. D.I. and Z.A. acknowledge the financial support of the National Fund for Scientific Research of Belgium, Grant No. 2.4587.99. D.I. is grateful to Digital Instruments/Veeco Metrology Group for the support of his stay in Santa Barbara, CA. The authors thank G. Bar for helpful comments on the resolution and contact mechanics of tapping mode, A. Jonas for enlightening discussions on the semicrystalline morphology and the code of a desmearing routine, N. Ono (Mitsubishi Materials Corp., Silicon Research Center) for kindly providing the numerical data on the temperature dependence of the elastic modulus of Si, and the referees for the careful consideration of the manuscript and useful remarks and suggestions.

References and Notes

(1) Zachmann, H. G.; Schmidt, G. F. *Makromol. Chem*. **1962**, *52*, 23. Elsner, G.; Zachmann, H. G.; Milch, J. R. *Makromol. Chem*. **1981**, *182*, 657. Elsner, G.; Koch, M. H. J.; Bordas, J.; Zachmann, H. G. *Makromol. Chem*. **1981**, *182*, 1262.
(2) Groeninckx, G.; Reynaers, H.; Berghmans, H.; Smets, G. *J. Polym. Sci., Polym. Phys. Ed*. **1980**, *18*, 1311. Groeninckx, G.; Reynaers, H. *J. Polym. Sci., Polym. Phys. Ed*. **1980**, *18*, 1325.
(3) Yamashita, Y. *J. Polym. Sci., Part A* **1965**, *3*, 81.
(4) Watkins, N. C.; Hansen, D. *Textile Res. J*. **1968**, *32* (4), 388.
(5) Ivanov, D. A.; Pop, T.; Yoon, D. Y.; Jonas, A. M. *Polym. Mater. Sci. Eng*. **1999**, *81*, 335.
(6) Chen, W.; Lofgren, E. A.; Jabarin, S. A. *J. Appl. Polym. Sci*. **1998**, *70*, 1965.
(7) Holdsworth, P. J.; Turner-Jones, A. *Polymer* **1971**, *12*, 195. Medellin-Rodriguez, F. J.; Phillips, P. J.; Lin, J. S.; Campos, R. *J. Polym. Sci., Polym. Phys*. **1997**, *35*, 1757.
(8) Everall, N.; et al. *Polymer* **1994**, *35*, 3184.
(9) Dinelli, F.; Assender, H. E.; Kirov, K.; Kolosov, O. V. *Polymer* **2000**, *41*, 4285.
(10) Ivanov, D. A.; Amalou, Z.; Magonov, S. N., manuscript in preparation.
(11) Zhou, W.; Cheng, S. Z. D.; Putthanarat, S.; Eby, R. K.; Reneker, D. H.; Lotz, B.; Magonov, S.; Hsieh, E. T.; Geerts, R. G.; Palackal, S. J.; Hawley, G. R.; Welch, M. B. *Macromolecules* **2000**, *33*, 6861.
(12) Hobbs, J. K.; Mcmaster, T. J.; Miles, M. J.; Barham, P. J. *Polymer* **1998**, *39*, 2437.
(13) Haubruge, H.; Jonas, A. M., personal communication.
(14) Sarid, D. *Scanning Force Microscopy with Applications to Electric, Magnetic, and Atomic Forces*; Oxford University Press: New York, 1991.
(15) Sader, J. E. *J. Appl. Phys*. **1998**, *84*, 64. Chon, J. W. M.; Mulvaney, P.; Sader, J. E. *J. Appl. Phys*. **2000**, *87*, 3978.
(16) Ono, N.; Kitamura, K.; Nakajima, K.; Shimanuki, Y. *Jpn. J. Appl. Phys*. **2000**, *39*, 368.
(17) Ivanov, D. A.; Daniels, R.; Magonov, S. N. Exploring the High-Temperature AFM and Its Use for Studies of Polymers. Application Note published by Digital Instruments/Veeco Metrology Group (2001). URL: http://di.com/AppNotes_PDFs/AN45%20HeatingStage.pdf.
(18) Basire, C.; Ivanov, D. A. *Phys. Rev. Lett*. **2000**, *85*, 5587.
(19) Pratt, W. K. *Digital Image Processing*, 2nd ed.; John Wiley & Sons: New York, 1991.
(20) Koberstein, J. T.; Morra, B.; Stein, R. S. *J. Appl. Crystallogr*. **1980**, *13*, 34.
(21) Glatter, O. *J. Appl. Crystallogr*. **1974**, *7*, 147.
(22) Strobl, G. R.; Schneider, M. *J. Polym. Sci., Part B* **1980**, *18*, 1343.
(23) Magonov, S. N.; Elings, V.; Whangbo, M.-H. *Surf. Sci*. **1997**, *375*, L385.
(24) Vonk, C. G. *J. Appl. Crystallogr*. **1978**, *11*, 541.
(25) Verma, R. K.; Hsiao, B. S. *Trends Polym. Sci*. **1996**, *4*, 312.
(26) It should be noted that the lamellar insertion growth would be much more effective in decreasing the SAXS long period as compared to the formation of separate stacks of thinner crystals. However, in some instances the insertion growth was found incompatible with SAXS data for high-temperature melt crystallization: Verma, R. K.; Velikov, V.; Kander, R. G.; Marand, H.; Chu, B.; Hsiao, B. S. *Polymer*. **1996**, *37*, 5357.
(27) Wang, Z. G.; Hsiao, B. S.; Fu, B. X.; Liu, L.; Yeh, F.; Sauer, B. B.; Chang, H.; Schultz, J. M. *Polymer* **2000**, *41*, 1791.

(28) Ivanov, D. A.; Legras, R.; Jonas, A. M. *Macromolecules* **1999**, *32*, 1582.

(29) The distance distributions determined from AFM images will be called "apparent" throughout the paper since the exact inclination of the crystalline lamellae with respect to the image plane is unknown. The effect of possible crystals inclination on the morphological parameters found from AFM is discussed further in the text.

(30) It is worth noting that a simple image cross-section analysis would not always provide a good estimate of the long period due to significant lamellar stacking disorder. It is thus important that all the data contained in the image (or several images) are treated at once to determine the statistically meaningful distance between the adjacent crystals.

(31) If one disregards the hypothesis of large amorphous gaps remaining in the semicrystalline structure after the completion of crystallization, which has not been supported experimentally, the bulk and linear crystallinities should be rather close, with the linear crystallinity being slightly higher for simple geometrical reasons.

(32) Glatter, O.; Kratky, O. *Small Angle X-ray Scattering*; Academic Press: London, 1982.

(33) Weihs, T. P.; Nawaz, Z.; Jarvis, S. P.; Pethica, J. B. *Appl. Phys. Lett.* **1991**, *59*, 3536.

(34) Sheyko, S. S. *Adv. Polym. Sci.* **2000**, *151*, 61.

(35) Ponomarenko, S. A.; Boyko, N. I.; Shibaev, V. P.; Magonov, S. N. *Langmuir* **2000**, *16*, 5487.

(36) Cabral, J. T.; Higgins, J. S.; McLeish, T. C. B.; Strausser, S.; Magonov, S. N. *Macromolecules* **2001**, *34*, 3748.

(37) Since the morphological parameters of the semicrystalline structure of PET are very sensitive to T_c in the high-temperature range employed in the experiment, the observed discrepancies between the values found from AFM and SAXS can result from a slight difference in the thermal history of the samples.

MA010809B